High Power Laser Science and Engineering, (2025), Vol. 13, e70, 11 pages.
doi:10.1017/hpl.2025.10052

HIGH POWER LASER SCIENCE AND ENGINEERING

RESEARCH ARTICLE

A 100 Hz, 4.71 mJ, 3.8 μm, narrow-linewidth, electro-optic *Q*-switched self-optical parametric oscillator based on Nd:MgO:PPLN crystal

Rui Zhao[1], Shuang Wu[1], Le Zhang[2], Hang Liu[1], Zijian Wang[1], Chao Wang[1], Yongji Yu[1], and Guangyong Jin[1]

[1]*Jilin Key Laboratory of Solid Laser Technology and Application, Changchun University of Science and Technology, Changchun, China*

[2]*School of Mathematics and Statistics, Changchun University of Science and Technology, Changchun, China*

(Received 20 February 2025; revised 23 May 2025; accepted 7 July 2025)

Abstract

This paper introduces a high single-pulse energy, narrow-linewidth mid-infrared self-optical parametric oscillator (mid-IR SOPO) with a cavity length of 120 mm and a Nd:MgO:PPLN crystal. To achieve high single-pulse energy and high peak power in mid-IR light sources, a $LiNbO_3$ electro-optic Q-switch (EOQ) is introduced for the first time in a mid-IR SOPO. A narrow-linewidth EOQ-SOPO rate equation is formulated, and experiments are conducted using a single Fabry–Pérot etalon. At a 500 μs pump pulse width, a 4.71 mJ single-pulse idler light at 3838.2 nm is achieved, with a linewidth of 0.412 nm, single-pulse width of 4.78 ns and peak power of 985 kW. At 200 μs, the idler light at 3845.2 nm exhibits a minimum linewidth of 0.212 nm.

Keywords: electro-optic *Q*-switch; mid-infrared; narrow linewidth; Nd:MgO:PPLN; self-optical parametric oscillator

1. Introduction

The mid-infrared (mid-IR) wavelength range of 3–5 μm represents a critical atmospheric window, as it can enable long-distance signal transmission owing to its excellent atmospheric penetration properties[1–4]. This wavelength range has been widely used in various fields, including atmospheric remote sensing, environmental monitoring, lidar, spectroscopy and electro-optical countermeasures[5–12]. High single-pulse energy mid-IR lasers can enhance the detection range in lidar applications and improve the success rate of electro-optical countermeasures such as interference, blinding and dazzling against detectors[13]. The introduction of narrow-linewidth characteristics in these lasers can reduce background noise and minimize detection errors, thereby improving lidar accuracy and detection sensitivity[14–17]. Recent advances in mid-IR nonlinear crystals and high-energy fundamental lasers have led to the optimization and development of high-energy mid-IR optical parametric oscillators (OPOs) such as MgO:PPLN-OPO, $KTiOPO_4$ (KTP)-OPO, $KTiOAsO_4$ (KTA)-OPO and $ZnGeP_2$ (ZGP)-OPO[18–20]. However, the complex structures of these systems pose challenges for the miniaturization of mid-IR lasers. Compared with the traditional superlattice material MgO:PPLN, the Nd:MgO:PPLN crystal, formed by polarizing Nd^{3+}-doped MgO:$LiNbO_3$ as a substrate, enables both fundamental light gain and pump-driven optical parametric frequency conversion within a single medium. This quasi-phase-matching self-OPO (QPM-SOPO) approach provides an effective technological pathway for simplifying mid-IR OPO systems and reducing their size and weight, facilitating the development of compact, single-pulse 3–5 μm mid-IR lasers.

High-energy fundamental light lasers are commonly used as the pump source for OPOs to generate near- and mid-IR lasers with high single-pulse energy[21–23]. However, these energy-accumulating mid-IR lasers exhibit various limitations such as large volume and multicomponent losses. Liu *et al.*[24] used two KTA crystals cut along different crystallographic orientations for phase matching, achieving idler light outputs of 24.6 mJ at 3.75 μm and 33.8 mJ at 3.46 μm at a repetition rate of 100 Hz. The spectral line widths were

Correspondence to: Y. Yu and G. Jin, Jilin Key Laboratory of Solid Laser Technology and Application, Changchun University of Science and Technology, Changchun 130022, China. Emails: yyjcust@163.com (Y. Yu); jgyciom@163.com (G. Jin)

approximately 61 and 93 nm for the wavelengths of 3.75 and 3.46 μm, respectively. However, the laser diode (LD) side-pumped neodymium-doped yttrium aluminum garnet (Nd:YAG) master oscillator power amplifier (MOPA) used as the pump source in this study occupied a significant amount of space. Fan *et al.*[25] used a Ho:YAG-MOPA system operating at 2 μm, delivering a total output energy of 138.3 mJ, as the pump source. By leveraging a ZGP-MOPA system, the authors achieved a mid-IR laser output of 71 mJ at a repetition rate of 300 Hz. The spectral linewidth of the 3.8 μm laser was approximately 129 nm. However, the ZGP-MOPA system included a ZGP-OPO master oscillator stage and two ZGP-OPOs, resulting in a complex system architecture that could not meet the spectral precision requirements for practical applications. The existing mid-IR lasers derived through MgO:PPLN-OPOs and Nd:MgO:PPLN-SOPOs typically exhibit high repetition rates, particularly in narrow-linewidth configurations. Using a Fabry–Pérot (F-P) etalon to narrow the linewidth of the fundamental or signal light in all-solid-state OPOs is a compact and effective method to indirectly compress the linewidth of idler light[26]. Xing *et al.*[27] developed a self-seeded PPMgLN-OPO pumped by a single longitudinal-mode laser at 1065 nm. This system achieved a narrow-linewidth mid-IR laser output at 3031 nm with a spectral linewidth of 0.35 nm and a repetition rate of 75 kHz. The corresponding single-pulse energy was 35.6 μJ. Lv *et al.*[28] demonstrated a narrow-linewidth mid-IR laser using a single F-P etalon within the OPO cavity to compress the linewidth of the signal light. This approach resulted in the generation of 3.74 μm idler light with a remarkably narrow linewidth of 0.3 nm. The system operated at a repetition frequency of 10 kHz, delivering a corresponding single-pulse energy of 212 μJ. Chen *et al.*[29] reported the first tunable eye-safe self-frequency-conversion laser, integrating the laser gain medium, EO *Q*-switch and parametric gain medium within a single Nd:MgO:PPLN with two-dimensional (2D) periodical poling. This system achieved an output energy of 3.3 μJ at 1525 nm, with a spectral linewidth of 2.8 nm. Wei *et al.*[30] introduced a compact L-cavity mid-IR self-optical parametric oscillator (SOPO) using an 808-nm LD for end-pumping, which was detuned from the absorption peak of the crystal. This system produced output energies of 32.8 μJ at 1.51 μm and 15.2 μJ at 3.86 μm, operating at a repetition frequency of 25 kHz. However, significant thermal effects were observed, leading to output saturation when the pump power reached 15.3 W. Wang *et al.*[31] used an F-P etalon to compress the linewidth of a 2168 nm degenerate wavelength in an SOPO. This approach achieved a narrowed linewidth of 2.23 nm, with a repetition frequency of 60 kHz and single-pulse energy of 10.8 μJ. Owing to the stringent polarization-matching condition (e+e→e) required for cascaded frequency conversion in Nd:MgO:PPLN-SOPO, thermal effects during the gain process generated σ-polarized (σ-pol) 1093 nm fundamental light (non-matching polarization). Although this polarization exhibited higher output power, it was detrimental to subsequent parametric frequency conversion, consequently, ensuring the dominance of π-polarized (π-pol) 1084 nm fundamental light gain across the entire pump region is crucial for achieving efficient and stable frequency conversion. Building on these advancements, our research group implemented a pulsed LD end-pumped coupling scheme to mitigate thermal effects at the crystal end face. By incorporating passive *Q*-switching within a compact short cavity, we achieved a single-pulse energy of 121 μJ at 3.81 μm, operating at a repetition frequency of 25.11 kHz[32]. This approach could effectively reduce thermal effects in Nd:MgO:PPLN crystals, providing a technical basis for improving the single-pulse energy of the SOPO. However, the single-pulse energy of narrow-linewidth OPOs is typically low, which limits their application in fields such as atmospheric sensing. To date, reports on high single-pulse energy, narrow-linewidth mid-IR lasers based on Nd^{3+}-doped $LiNbO_3$ substrates remain scarce. Table 1 presents the parameters of representative pulsed mid-IR OPO systems.

Therefore, in this study, we investigate a 100 Hz narrow-linewidth SOPO using an 813 nm LD end-pumped Nd:MgO:PPLN crystal, adopting $LiNbO_3$ as a *Q*-switch crystal for pulse-off *Q*-switching for the first time. A mathematical model of the electro-optic *Q*-switch (EOQ)-SOPO rate equation under pulsed pumping is established to simulate the temporal evolution of the upper-level population and photon numbers of the three waves under pulsed pumping combined with EOQ-switching, revealing the temporal characteristics of the three waves. Subsequently,

Table 1. Representative pulsed mid-IR OPO systems.

Pump source	OPO crystal	Output power/energy @wavelength	Reference and year
1064 nm, Nd:YAG-MOPA, 100 Hz	KTA	24.6 mJ @3.75 μm; 33.8 mJ @3.46 μm	[24] 2013
2090 nm, Ho:YAG-MOPA, 300 Hz	ZGP	71 mJ @3.8 μm	[25] 2024
1065 nm, Yb-doped fiber laser, 75 kHz	MgO:PPLN	35.6 μJ @3.03 μm	[27] 2017
1064 nm, Nd:YAG laser, 10 kHz	MgO:PPLN	212 μJ @3.74 μm	[28] 2023
808 nm, LD, continuous wave (CW)	Nd:MgO:PPLN	3.3 μJ @1.525 μm	[29] 2012
810 nm, LD, CW	Nd:MgO:PPLN	15.2 μJ @3.86 μm	[30] 2022
813 nm, LD, CW	Nd:MgO:PPLN	10.8 μJ@2.168 μm	[31] 2024
813 nm, LD, 30 Hz	Nd:MgO:PPLN	121 μJ@3.81 μm	[32] 2024

https://doi.org/10.1017/hpl.2025.10052 Published online by Cambridge University Press

experiments are conducted on 100 Hz EOQ-switched fundamental light and idler light to explore the output performance of the EOQ-SOPO under different pump pulse widths. An F-P etalon is inserted into the fundamental cavity to compress the linewidth of the fundamental light, thereby indirectly narrowing the linewidth of the idler light. Ultimately, in the 100 Hz narrow-linewidth EOQ-SOPO, narrow-linewidth 3845.2 nm idler light is obtained at a pump pulse width of 200 μs, corresponding to a minimum linewidth of 0.212 nm. At 500 μs, a 4.71 mJ single-pulse idler light at 3838.2 nm is achieved, with a linewidth of 0.412 nm, single-pulse width of 4.78 ns and peak power of 985 kW.

2. Theoretical analysis

2.1. Narrow-linewidth EOQ-SOPO rate equation model

The generation of nanosecond pulses in pulsed-pumped EOQ-SOPOs can be described using three-wave coupled rate equations (Equations (1)–(7)). Throughout the evolution of the laser pulse, it is assumed that the photon density inside the cavity follows a plane-wave approximation[33–36]:

$$\frac{\mathrm{d}N(t)}{\mathrm{d}t} = R_{\mathrm{in}}(\mathrm{t}) - \gamma c\sigma N(t)\varphi_{\mathrm{j}}(t) - \frac{N(t)}{\tau}, \tag{1}$$

$$\frac{\mathrm{d}\varphi_{\mathrm{j}}(t)}{\mathrm{d}t} = \sigma c\frac{l_{\mathrm{cry}}}{l_{\mathrm{cav}}}N(t)\varphi_{\mathrm{j}}(t) - g\frac{l_{\mathrm{cry}}}{l_{\mathrm{OPO}}}\varphi_{\mathrm{j}}(t)\varphi_{\mathrm{s}}(t) - \frac{1}{\tau_{\mathrm{j}}'}\varphi_{\mathrm{j}}(t) + \Delta P_{\mathrm{j}}\varphi_{\mathrm{j}}(t), \tag{2}$$

$$\frac{\mathrm{d}\varphi_{\mathrm{s}}(t)}{\mathrm{d}t} = g\frac{l_{\mathrm{cry}}}{l_{\mathrm{OPO}}}\varphi_{\mathrm{j}}(t)\varphi_{\mathrm{s}}(t) - \frac{1}{\tau_{\mathrm{s}}}\varphi_{\mathrm{s}}(t) + \Delta P_{\mathrm{s}}\varphi_{\mathrm{s}}(t), \tag{3}$$

$$\frac{\mathrm{d}\varphi_{\mathrm{id}}(t)}{\mathrm{d}t} = \frac{2\hbar\mu_0 d_{\mathrm{eff}}^2\omega_{\mathrm{j}}\omega_{\mathrm{s}}\omega_{\mathrm{id}}l_{\mathrm{cry}}^2}{n_{\mathrm{j}}^2 n_{\mathrm{s}}^2}\varphi_{\mathrm{p}}(t)\varphi_{\mathrm{s}}(t) + \frac{1}{\tau_{\mathrm{id}}}\varphi_{\mathrm{id}}(t), \tag{4}$$

$$g = \frac{\hbar\omega_{\mathrm{j}}\omega_{\mathrm{s}}\omega_{\mathrm{id}}d_{\mathrm{eff}}^2 l_{\mathrm{cry}}}{\varepsilon_0 c n_{\mathrm{j}}^2 n_{\mathrm{s}}^2 n_{\mathrm{id}}}, \tag{5}$$

$$\Delta P_{\mathrm{j}} = \frac{1}{2}\frac{c}{n_{\mathrm{j}}}\frac{1}{2l_{\mathrm{cav}}}\frac{1}{F_{\mathrm{pth}}}, \quad \Delta P_{\mathrm{s}} = \frac{1}{2}\frac{c}{n_{\mathrm{s}}}\frac{1}{2l_{\mathrm{OPO}}}\frac{1}{F_{\mathrm{pth}}}, \tag{6}$$

$$F_{\mathrm{pth}} = \frac{2n_{\mathrm{j}}n_{\mathrm{s}}n_{\mathrm{id}}c^3\varepsilon_0(1-R_{\mathrm{s}})\left(1+\frac{\alpha_{\mathrm{id}}l_{\mathrm{cry}}}{3}\right)}{h\omega_{\mathrm{j}}\omega_{\mathrm{s}}\omega_{\mathrm{id}}d_{\mathrm{eff}}^2 l_{\mathrm{cry}}^2}\frac{\pi\left({w_{\mathrm{s}}}^2+{w_{\mathrm{j}}}^2\right)}{2}, \tag{7}$$

where $N, \varphi_{\mathrm{j}}, \varphi_{\mathrm{s}}$ and φ_{id} denote the population inversion density, fundamental photon density, signal photon density and idler photon density, respectively, c is the speed of light, σ denotes the stimulated emission cross-section of the crystal, τ is the lifetime of the upper energy level, γ represents the inversion factor, l_{cry}, l_{OPO} and l_{cav} are the lengths of the nonlinear crystal, optical parametric oscillation cavity and total resonator, respectively, g is the gain coefficient for the signal and idler waves during parametric oscillation, ω_{j}, ω_{s} and ω_{id} represent the angular frequency of the fundamental, signal and idler waves, w_{j} and w_{s} represent the beam spot radii for the fundamental and signal waves, respectively, d_{eff} is the effective nonlinear coefficient of the crystal, $n_{\mathrm{j}}, n_{\mathrm{s}}$ and n_{i} denote the refractive indices of the three waves, h represents Planck's constant, where $\hbar = h/2\pi$, ΔP_{j} and ΔP_{s} denote the spontaneous emission terms for the fundamental and signal waves, respectively, and F_{pth} indicates the resonator threshold; the signal light oscillates only when the photon density of the fundamental wave exceeds this threshold. Further, α_{id} is the absorption coefficient of the crystal at the idler wavelength. In this model, external square-wave modulation is introduced, and the pump term $R_{\mathrm{in}}(t)$ can be expressed as follows:

$$R_{\mathrm{in}}(\mathrm{t}) = \frac{P_{\mathrm{in}}\left[1-\exp\left(-\alpha_{\mathrm{LD}}l_{\mathrm{cry}}\right)\right]}{\hbar\nu_{\mathrm{LD}}\frac{\pi w_{\mathrm{LD}}^2}{2}l_{\mathrm{cry}}}s(t), \tag{8}$$

$$s(t) = 1 + A_{\mathrm{c}}\cdot\mathrm{square}\left(2\pi f_{\mathrm{c}}t, \mathrm{Ratio}\right), \tag{9}$$

where P_{in} is the injected power of the pump source, α_{LD} is the absorption coefficient of the laser crystal for the pump light, $\hbar\nu_{\mathrm{LD}}$ denotes the energy of a single photon emitted by the laser pump source, w_{LD} is the beam radius of the pump source, A_{c} represents the modulation depth, f_{c} is the external control frequency and Ratio indicates the duty cycle of the pump. As active Q-switching affects only the intracavity loss of the fundamental wave, we simply need to add the Q-switching term to the total loss. The Q-switching term $T_{\mathrm{j}}(t)$ is represented by a step function and, thus, the total intracavity loss of the fundamental light τ_{j} can be expressed as follows:

$$\tau_{\mathrm{j}} = \frac{t_{\mathrm{rj}}}{L_{\mathrm{j}} + T_{\mathrm{j}}(t) + \ln\left(\frac{1}{R_{\mathrm{j}}}\right)}, \tag{10}$$

$$T_{\mathrm{j}}(t) = \begin{cases} T_1, & t+\Delta t-(t/P)\cdot P < P - t_{\mathrm{q1}}, \\ T_2, & t+\Delta t-(t/P)\cdot P > P - t_{\mathrm{q1}}, \end{cases} \tag{11}$$

where T_1 and T_2 represent the high-level (closed state) and low-level (open state) losses of the Q-switch, respectively, Δt is the delay time between the onset of the Q-switching signal and pump pulse signal, P denotes the period of the Q-switch and t_{q1} is the closing time of the Q-switch.

When an F-P etalon is introduced into the fundamental wave cavity, the intracavity loss increases. The loss of the F-P etalon $L_{\mathrm{F-P}}$ can be expressed as follows:

https://doi.org/10.1017/hpl.2025.10052 Published online by Cambridge University Press

$$L_{F-P} = -\ln\left[(1-R_{F-P})\,T_{F-p}\right], \tag{12}$$

$$T_{F-P} = \left[1+\frac{4R_{F-P}}{(1-R_{F-P})^2}\sin^2\left(\frac{2\pi n_{F-P}h_{F-P}\cos\theta}{\lambda}\right)\right]^{-1}, \tag{13}$$

where T_{F-P} is the transmission formula of the F-P etalon, R_{F-P} is the reflectivity of the F-P etalon, h_{F-P} is the thickness, n_{F-P} is the refractive index of the etalon and θ is the insertion angle of the F-P etalon. Therefore, τ_j' is the total intracavity loss of the narrow-linewidth fundamental light, which can be defined as follows:

$$\tau_j' = \frac{t_{rj}}{L_j + T_j(t) + L_{F-P} + \ln\left(\frac{1}{R_j}\right)}, \tag{14}$$

$$t_{rj} = \frac{2n_j l_{cav}}{c}\frac{1}{1-R_j}, \tag{15}$$

where τ_s and τ_{id} denote the total intracavity losses of signal and idler light photons, respectively:

$$\tau_s = \frac{t_{rs}}{L_s + \ln\left(\frac{1}{R_s}\right)}, \quad \tau_{id} = \frac{t_{rid}}{L_{id} + \ln\left(\frac{1}{R_{id}}\right)}, \tag{16}$$

$$t_{rs} = \frac{2n_s l_{OPO}}{c}\frac{1}{1-R_s}, \quad t_{rid} = \frac{2n_{id} l_{OPO}}{c}\frac{1}{1-R_{id}}, \tag{17}$$

where t_{rj}, t_{rs} and t_{rid} represent the cavity lifetimes of the fundamental, signal and idler lights, respectively, L_j, L_s and L_{id} are the round-trip intrinsic losses of the fundamental, signal and idler lights, respectively, and R_j, R_s and R_{id} denote the reflectivities of the fundamental, signal and idler light cavity mirrors, respectively.

2.2. Simulation results of the narrow-linewidth EOQ-SOPO rate equation model

The rate equation is solved numerically using the fourth-order Runge–Kutta method. The pump light wavelength is set to 813 nm, with fundamental, signal and idler wavelengths set as 1084, 1510 and 3840 nm, respectively. The pump power is 250 W and the main parameters are listed in Table 2. Figure 1(a) shows the simulation results for the pulse sequence of a narrow-linewidth EOQ-SOPO with a 200 μs pump pulse width. The results show the dynamic evolution of N, φ_j, φ_s and φ_{id} over time. In the early stages of the pump pulse, N is higher, leading to significant relaxation oscillations in φ_j. The pulses of the signal and idler waves are strictly synchronized with a repetition frequency of 100 Hz, demonstrating high temporal stability and periodicity. Figure 1(b) shows the simulation results of a single pulse for the three waves, reflecting the microsecond-level dynamic evolution of, φ_j, φ_s and φ_{id} over time. During the laser output process, at 200 μs, N rapidly decreases, leading to a sharp increase in φ_j to a peak, followed by a gradual decay. At 200.02 μs, φ_s and φ_{id} begin oscillating, with φ_{id} pulses forming earlier and rapidly decaying, demonstrating the rapid release of intracavity gain.

Table 2. EOQ-SOPO rate equation model parameters.

Symbol	Value	Symbol	Value
τ (μs)	100	n_s	2.13
σ (cm^{-3})	5.1×10^{-19}	n_{id}	2.05
γ	1	R_j	0.99
l_{cry} (mm)	30	R_s	0.99
l_{OPO} (mm)	40	R_{id}	0.01
l_{cav} (mm)	120	T_1	0.98
d_{eff} (pm/V)	16	T_2	0
n_j	2.15	tq_1 (ns)	20

Figure 1(c) illustrates the temporal evolution of the first fundamental pulse at different pump energies. Figure 1(d) presents the temporal evolution of the first idler pulse at different pump energies. In the simulation, φ_{id} is based on the consumption of φ_j, which increases with longer pump pulse durations. Since the idler light does not participate in resonant oscillation during the parametric conversion process, its effective cavity lifetime is shorter, resulting in a narrower pulse width.

Figure 2(a) shows the simulation results for the single-pulse widths of free-running and narrow-linewidth fundamental lights under different pump pulse widths (200, 300, 400 and 500 μs). The single-pulse widths of free-running fundamental lights are 34.8, 32.6, 31.5 and 28.1 ns. The corresponding values for narrow-linewidth fundamental lights are 24.5, 24.0, 22.3 and 21.9 ns, significantly smaller than those in the free-running state. Figure 2(b) shows the single-pulse widths of free-running and narrow-linewidth idler lights under varying pump pulse widths. The single-pulse widths of free-running idler lights are 7.5, 7.0, 6.2 and 5.7 ns, while those of narrow-linewidth idler lights are 4.6, 4.3, 3.8 and 2.7 ns. Compared with free-running, narrow-linewidth idler lights exhibit smaller pulse widths, and the values in both modes decrease as the pump pulse width increases. These results indicate that the laser pulse width is significantly influenced by the pump pulse width under free-running and narrow-linewidth modes. The proposed mathematical model provides a theoretical basis for understanding the dynamic behavior and photon density distribution characteristics of the narrow-linewidth EOQ-SOPO. Moreover, it offers theoretical guidance for optimizing experimental parameters, improving laser performance and performing system design and optimization.

https://doi.org/10.1017/hpl.2025.10052 Published online by Cambridge University Press

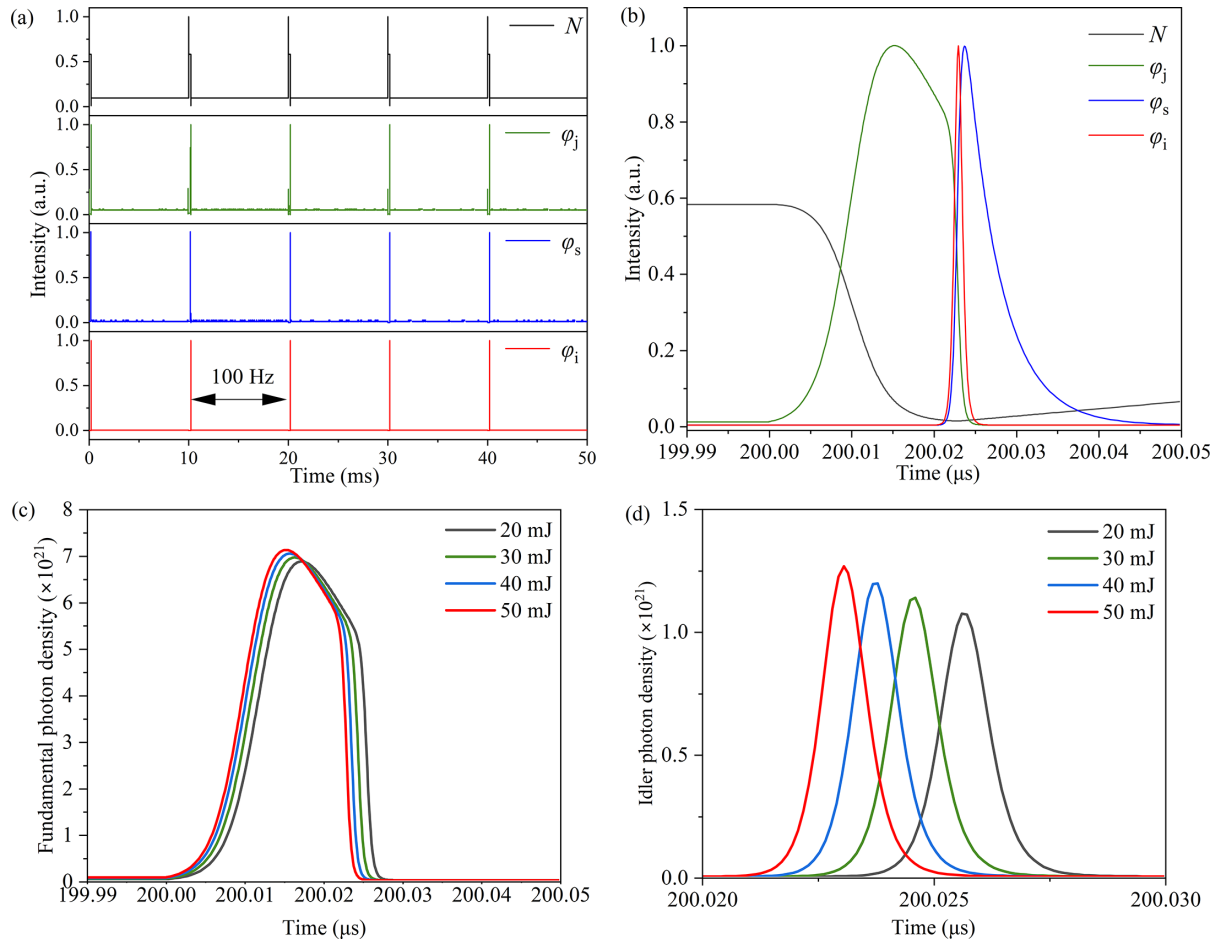

Figure 1. Simulation results of the rate equations for the narrow-linewidth EOQ-SOPO with a pump pulse width of 200 μs: (a) pulse sequence; (b) enlarged first pulse; (c) the temporal evolution of the first fundamental pulse; (d) the temporal evolution of the first idler pulse.

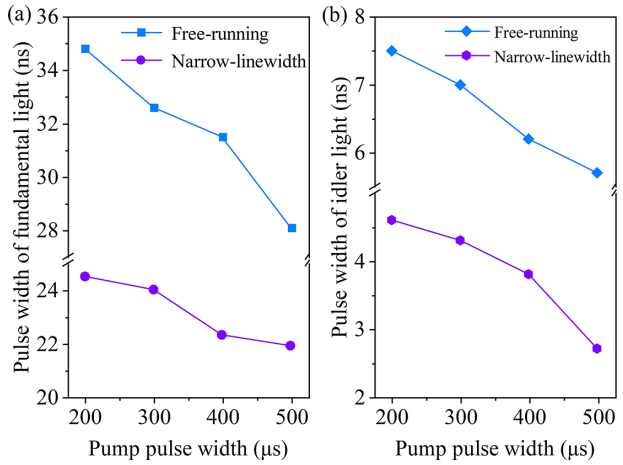

Figure 2. Simulated single-pulse widths for free-running and narrow-linewidth modes: (a) fundamental light; (b) idler light.

3. Experimental setup

Figure 3(a) schematically illustrates the experimental setup for the EOQ narrow-linewidth 1084 nm fundamental light based on Nd:MgO:PPLN. The fundamental resonator features a plano-concave cavity with a cavity length of 120 mm, formed by M_1 and M_2. The input mirror M_1 is a plane mirror coated with a high-transmission (HT, $T > 99\%$) film for 790–820 nm and a high-reflection (HR, $R > 99\%$) film for 1060–1095 nm. The output mirror M_2 is coated with HT ($T = 6\%$, $R = 300$ mm) film for 1084 nm. P is a 45° polarizer, coated with a polarization film for 1084–1093 nm (HT for π-pol and HR for σ-pol). Figure 3(b) presents a schematic of the experimental setup for the EOQ narrow-linewidth mid-IR SOPO based on Nd:MgO:PPLN. Figure 3(c) shows the physical experimental setup for the EOQ 100 Hz narrow-linewidth mid-IR SOPO. In this composite resonator, the fundamental cavity is formed by M_3 and M_5 with a cavity length of 120 m, while the OPO cavity is formed by M_3 and M_4 with a length of 40 mm. A plane mirror M_3 is used as an input mirror, coated with HT ($T > 99\%$) film for 813 nm and HR ($R > 99\%$) films for 1084, 1400–1650 and 3400–4200 nm. The output mirror M_4 of the parametric oscillation cavity is a plane mirror coated with HT ($T > 99\%$) film for 1084 nm, HR ($R > 99\%$) film for 1400–1700 nm and HT ($T > 99\%$) film for 3200–4000 nm. The total reflection mirror M_5 is coated with HR ($R > 99\%$,

https://doi.org/10.1017/hpl.2025.10052 Published online by Cambridge University Press

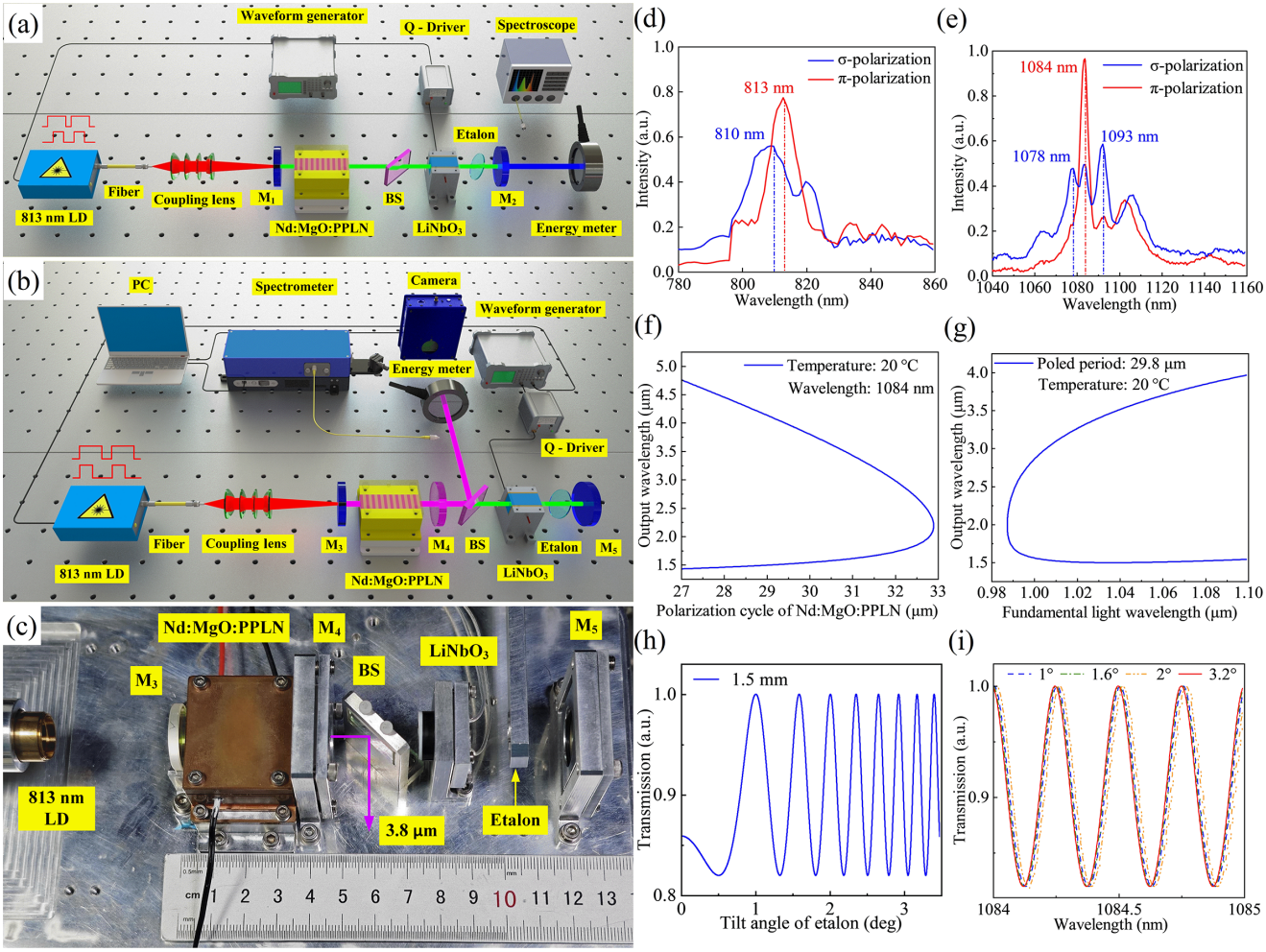

Figure 3. (a) Experimental setup for 100 Hz narrow-linewidth EOQ 1084 nm fundamental laser. (b) Experimental setup for 100 Hz narrow-linewidth EOQ-SOPO. (c) Physical experimental setup for 100 Hz narrow-linewidth EOQ-SOPO. (d) Absorption spectrum of the Nd:MgO:PPLN crystal. (e) Fluorescence emission spectrum of the Nd:MgO:PPLN crystal. (f) Polarization period tuning curve of the Nd:MgO:PPLN crystal. (g) Fundamental wavelength tuning curve of the Nd:MgO:PPLN crystal. (h) Transmittance–angle curve for a 1.5-mm-thick F-P etalon. (i) Relationship between transmittance and wavelength at different angles for a 1.5-mm-thick F-P etalon.

$R = 300$ mm) film for 1084 nm. A 45° polarization beam splitter (BS) is used, coated with a polarization film for 1084–1093 nm (HT for P-pol and HR for S-pol) and HR ($R > 99\%$) film for 3500–4200 nm.

Figure 3(d) shows the absorption spectrum of the Nd:MgO:PPLN crystal. Figure 3(e) shows the fluorescence emission spectrum of the Nd:MgO:PPLN crystal[37]. An 813 nm LD system (TY-ME30-813 nm) is used as the pump source. The pump light is delivered through an optical fiber (200 μm diameter, numerical aperture of 0.22) and focused through a 1:4 coupling lens system (model COFC-808-F400-22-4×, LENSTEK LASER OPTICS) to pump the end face of the Nd:MgO:PPLN crystal. The Nd:MgO:PPLN crystal is cut along the *a*-axis and doped with Nd^{3+} ions (0.4%, atom fraction) and MgO ions (5%, mole fraction). The crystal has a polarization period of 29.8 μm, with a grating duty cycle ranging between 0.4 and 0.6. The grating uniformity near the center of the crystal is superior to that near the edges. After precision polishing, the parallelism and flatness of the crystal surfaces are better than 30″ and $\lambda/6$, respectively. Both ends of the crystal are coated with anti-reflective (AR) coatings optimized for wavelength ranges of 790–820, 1060–1090, 1400–1700 and 3400–4200 nm. The crystal is wrapped in indium foil and placed in a copper crystal holder. Precise temperature control is achieved using a combination of thermoelectric cooling plates and a water-cooling system, with a temperature control accuracy of ±0.01°C. During the experiments, the temperature is maintained at 20°C. Figure 3(f) shows the polarization period tuning curve of the Nd:MgO:PPLN crystal. Figure 3(g) shows the fundamental wavelength tuning curve of the Nd:MgO:PPLN crystal[38].

A 1.5-mm-thick F-P fused silica solid etalon (produced by DIEN, China) is placed in the fundamental cavity. The angle of the etalon is controlled using a custom high-precision optical adjustment mount. As shown in Figure 3(h), the transmission of the F-P etalon varies with the angle,

https://doi.org/10.1017/hpl.2025.10052 Published online by Cambridge University Press

exhibiting HT at angles of 1°, 1.6°, 2°, 2.4°, 2.7°, 2.9°, 3.2° and 3.4°. Figure 3(i) shows the transmission of the 1.5-mm-thick F-P etalon as a function of wavelength, revealing HT at the 1084 nm fundamental wavelength across different angles.

$LiNbO_3$ is used as the EOQ-switching crystal. The electrode surfaces of the crystal are coated with gold electrodes for voltage application, with dimensions of 7 mm × 7 mm × 15 mm, and the optical surfaces are coated with 1084 nm AR coatings. The pulse-off *Q*-switch driver applies a depolarization signal with a falling edge duration of approximately 12 ns and a voltage of 3 kV. A pulse/arbitrary waveform generator (SDG6032X, SIGLENT, China) is used to adjust the depolarization timing for time-domain synchronization with the LD pulse waveform.

The output energy is measured using a laser energy sensor (PE50BB, Ophir, Israel). The fundamental wavelength characteristics are measured using an optical spectrum analyzer (AQ6373, 350–1200 nm, Yokogawa, Japan). The idler wavelength characteristics are acquired using a spectrometer (waveScan-MIR, 1500–6300 nm, APE, Germany). The pulse temporal characteristics of the fundamental light are recorded using a silicon-biased detector (DET10A2, Thorlabs, USA). The pulse timing characteristics are measured using a pulse width detector (PCI3TE-12, VIGO Photonics, Poland) connected to an oscilloscope (MDO3054, Tektronix). The laser beam profile is captured using a pyroelectric array camera (Pyrocam III-HR, Ophir, Israel).

4. Results and discussion

4.1. The 100 Hz narrow-linewidth 1084 nm laser

In the fundamental light experiment, the pump source pulse signal is a square wave, the repetition frequency is 100 Hz and the pulse width is set as 200, 300, 400 and 500 μs. The repetition frequency of the EOQ switch is synchronized with the pump source at 100 Hz. The delay between the electro-optic modulation signal and pump pulse signal is adjusted accordingly. The falling edge of the depressurization signal is consistent with that of the pump pulse signal.

As shown in Figure 4(a), the output energy of the free-running 1084 nm fundamental light at different pulse widths varies with the pump energy. The maximum output energy obtained at pump pulse widths of 200, 300, 400 and 500 μs is 9.69, 14.62, 18.73 and 20.96 mJ, respectively, corresponding to pump energy values of 50, 75, 100 and 125 mJ. Overall, the laser output energy increased linearly with the increase in the pump energy. Figure 4(b) shows the relationship between the output energy of the fundamental light with a narrow linewidth of 1084 nm and the pump energy. The maximum output energy corresponding to different pump pulse widths is 6.95, 10.96, 14.25 and 15.94 mJ.

A comparison of the output energy of the 1084 nm fundamental light with the pump energy after free-running and narrowing shows that under the same pump conditions, the output energy of the free-running fundamental light is higher than that after narrowing. This loss of output energy is attributable to the increase in the cavity insertion loss owing to the F-P etalon frequency selective device placed in the cavity during spectral narrowing. The maximum output energy increases significantly with the increase in pulse width, indicating that a larger pump pulse width can improve the energy storage and release efficiency of the gain medium. At a pulse width of 200 μs, the difference between the maximum output energies of free-running and narrowed lights is small. At 500 μs, this difference increases, indicating that the efficiency loss of the narrowing process is more pronounced under high pump energy conditions.

Figure 5(a) shows the variation in the spectrum of the fundamental light without linewidth narrowing under different pump pulse widths. The peak wavelengths of the spectrum change slightly with the increase in pulse width, measured at 1084.90, 1084.89, 1084.57 and 1084.96 nm. The full-width at half-maximum (FWHM) values of fundamental light were directly read from the spectrometer by the THRESH method. The corresponding FWHM values are 0.1005, 0.1263, 0.1628 and 0.1889 nm. By introducing an F-P etalon into the fundamental frequency optical cavity and adjusting its angle to 3.2°, the fundamental light with the narrowest linewidth is obtained. Figure 5(b) shows the fundamental light spectrum

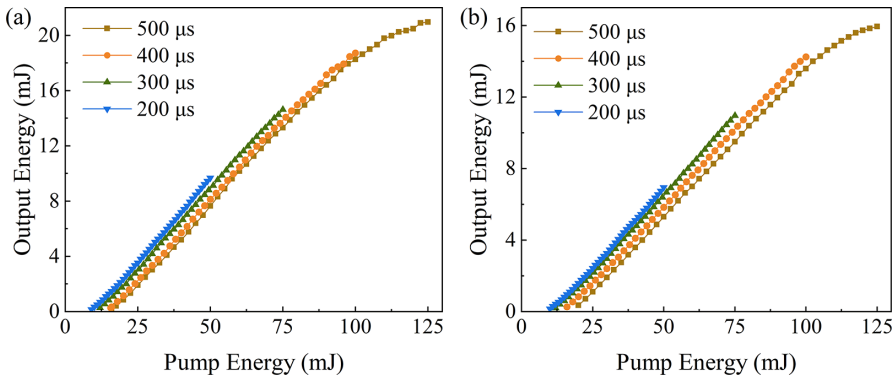

Figure 4. (a) The output energy of the free-running fundamental light. (b) The output energy of the narrow-linewidth fundamental light.

https://doi.org/10.1017/hpl.2025.10052 Published online by Cambridge University Press

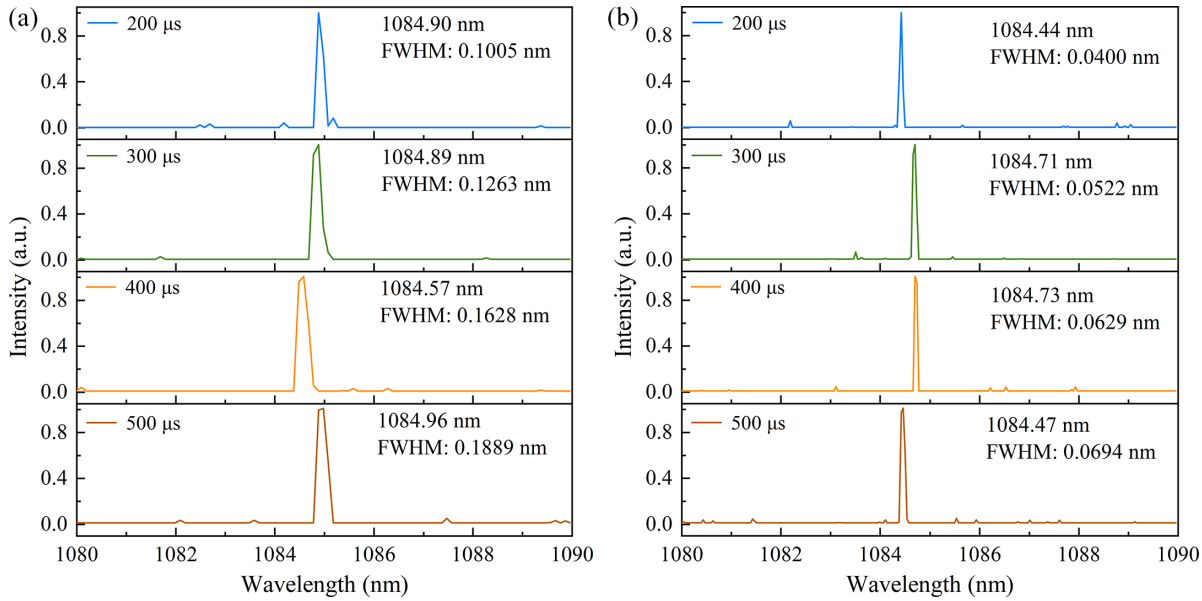

Figure 5. Relationship between the spectrum of the fundamental light and pump pulse width. (a) Free-running mode. (b) Narrow-linewidth mode.

compressed by the F-P etalon. Under different pump pulse widths, the spectral peaks are at 1084.44, 1084.71, 1084.73 and 1084.47 nm, showing minor deviations from the free-running peak wavelengths. After narrowing, the FWHM reduces to 0.0400, 0.0522, 0.0629 and 0.0694 nm. The F-P etalon exhibits a pronounced narrowing effect on the spectral linewidth of the fundamental light, achieving a compression ratio exceeding 60% and thereby providing an effective foundation for the indirect compression of idler light's linewidth.

Figure 6(a) shows the time-domain characteristics of the free-running fundamental light at 100 Hz with different pump pulse widths. With increasing pump pulse width, pulse widths of 32.86, 28.33, 27.15 and 26.48 ns are obtained. Figure 6(b) shows the time-domain characteristics of the narrow-linewidth fundamental light corresponding to different pump pulse widths at 100 Hz. With increasing pump pulse width, pulse widths of 26.47, 25.67, 24.30 and 21.40 ns are obtained. These results indicate that linewidth narrowing reduces the pulse width of the fundamental light.

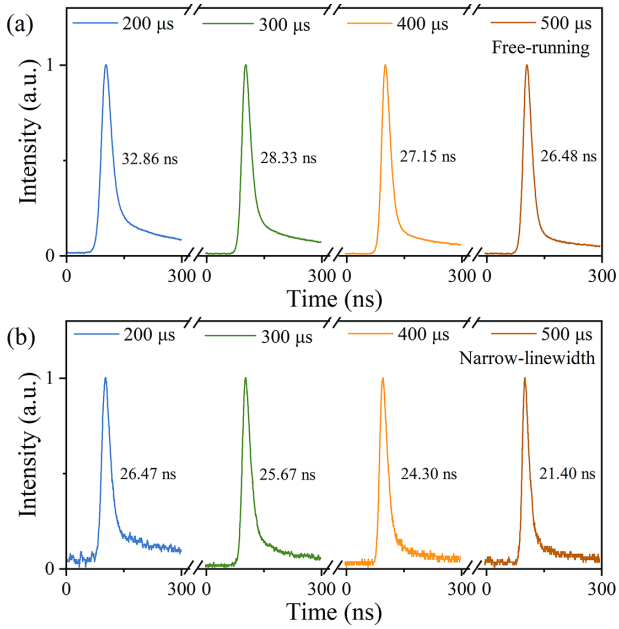

Figure 6. (a) Free-running 1084 nm pulse characteristics. (b) Narrow-linewidth 1084 nm pulse characteristics.

4.2. The 100 Hz narrow-linewidth EOQ-SOPO

Following the experimental study of fundamental light, experiments are conducted on the SOPO in the mid-IR range. As shown in Figure 7(a), the output energy of the free-running idler light exhibits a linear increase with the pump energy. The maximum output energy recorded at different pump pulse widths is 2.61, 4.01, 5.40 and 6.85 mJ, corresponding to pump energy values of 50, 75, 100 and 125 mJ, respectively. Figure 7(b) shows the relationship between the output energy of the narrow-linewidth idler light and pump energy. The maximum output energy recorded at different pulse widths is 1.77, 2.67, 3.58 and 4.71 mJ. A longer pump pulse width significantly increases the output energy, regardless of the mode (free-running or narrowing). However, the output energy in the narrowing mode is lower than that in the free-running mode. The energy difference gradually expands with the increase in the pulse width. As shown in Figure 8, we tested the output energy stability of the narrow-linewidth EOQ-SOPO in 30 min. The output energy fluctuation was 0.51% in RMS (root mean square).

https://doi.org/10.1017/hpl.2025.10052 Published online by Cambridge University Press

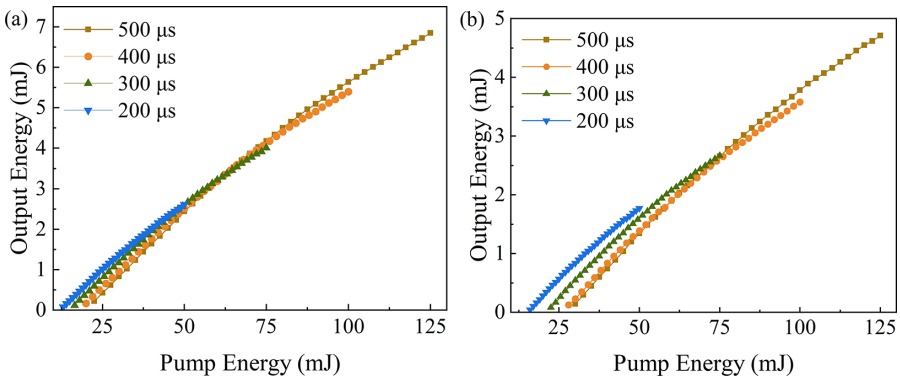

Figure 7. (a) The output energy of the free-running idler light. (b) The output energy of the narrow-linewidth idler light.

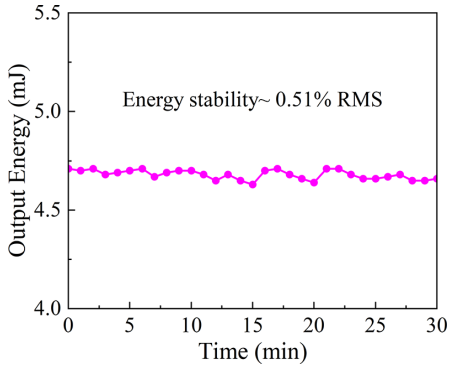

Figure 8. Energy stability of the narrow-linewidth EOQ-SOPO in 30 min.

Figure 9(a) shows the spectral distribution of the EOQ-SOPO output under different pump pulse widths. The central wavelengths are 3845.03, 3841.8, 3840.5 and 3838.4 nm. The FWHM values of idler light were obtained directly from the wavelength meter using a peak-to-valley fitting method. Corresponding FWHM values are 0.833, 0.865, 0.916 and 1.157 nm. The FWHM values for the free-running mode are larger. The central wavelength shifts toward a shorter wavelength with the increase in the pump pulse width. A larger pump pulse width likely results in heat accumulation and associated temperature-tuning effects. Concurrently, the spectral linewidth broadens due to enhanced nonlinear gain, because of higher fundamental energy at longer pump durations. The output spectrum after narrowing under different pump pulse widths is shown in Figure 8(b). The center wavelengths are 3845.2, 3841.2, 3840.4 and 3838.2 nm, with corresponding FWHM values of 0.212, 0.271, 0.304 and 0.412 nm, respectively. The spectral width and purity of the narrowed spectrum are significantly improved, especially in the short wavelength region. The linewidth reduces from 1.157 to 0.412 nm, and the compression range is 64%. These results demonstrate the effectiveness of indirect narrowing in optimizing the output spectrum for the mid-IR SOPO.

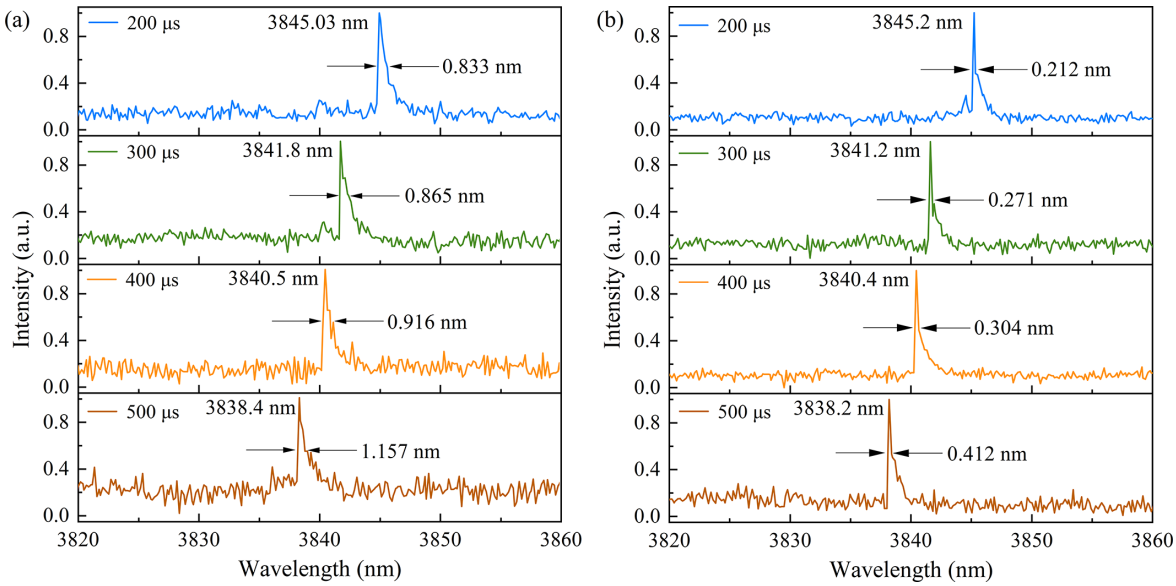

Figure 9. Output spectrum of the EOQ-SOPO: (a) free-running mode; (b) narrow-linewidth mode.

https://doi.org/10.1017/hpl.2025.10052 Published online by Cambridge University Press

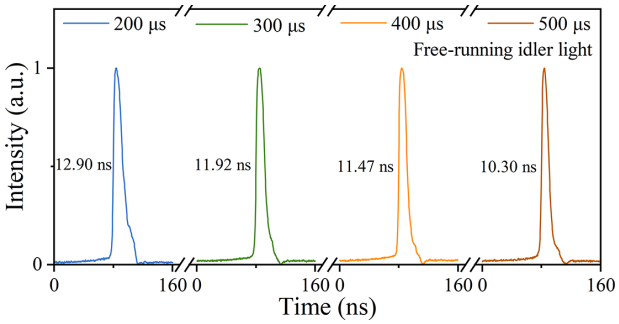

Figure 10. Single-pulse width of the free-running EOQ-SOPO.

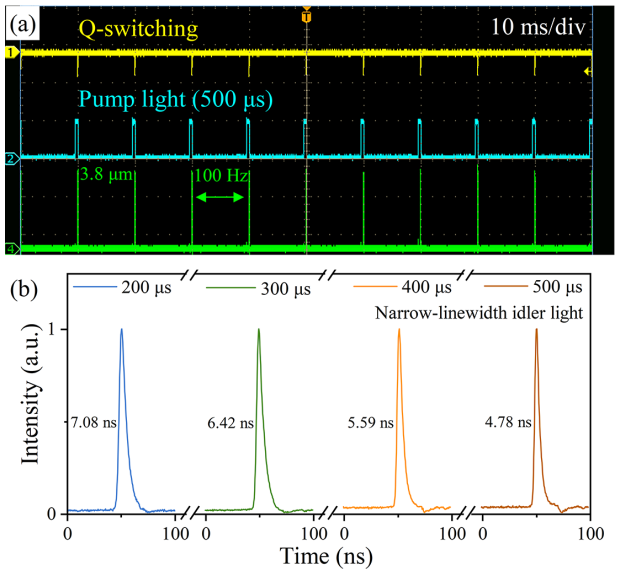

Figure 11. Pulse characteristics of the narrow-linewidth EOQ-SOPO. (a) Pulse sequence at a pump pulse width of 500 μs. (b) Single-pulse width under different pump pulse widths.

Figure 10 shows the single-pulse characteristics of free-running idler light under different pump pulse widths at a repetition frequency of 100 Hz. As the pump pulse width increases, the single-pulse width of the idler light gradually decreases. For pump pulse widths of 200, 300, 400 and 500 μs, the single-pulse widths are 12.90, 11.92, 11.47 and 10.30 ns, respectively. This trend is attributable to the gain dynamics and extraction efficiency of the cavity energy. The increase in the pump pulse width leads to enhanced gain saturation and increases the energy stored in the cavity, thus compressing the output pulse width. In addition, the maximum peak powers of the free-running idler light reach 202, 336, 471 and 665 kW.

Figure 11 shows the pulse characteristics of a narrow-linewidth mid-IR EOQ-SOPO. Figure 11(a) shows the pulse sequence waveform at a pump pulse width of 500 μs and a repetition frequency of 100 Hz. The mid-IR idler light pulse signal is strictly synchronized with the EOQ-switch signal, and the pulse shape is uniform and stable. Figure 11(b) shows the single-pulse time-domain waveforms and corresponding pulse widths under different pump pulse widths, measured to be 7.08, 6.42, 5.59 and 4.78 ns. In addition, the maximum peak powers of free-running idler light reach 250, 416, 640 and 985 kW. Although the obtained single-pulse width is larger than the theoretical results, the overall trend remains consistent.

A focusing mirror with a focal length of 150 mm is placed behind the BS mirror, and the size of the focused 3.8-μm idler light spot is measured using the knife-edge method. The beam profile curve is fitted according to the Gaussian beam propagation equation, with the results shown in Figure 12. Figures 12(a) and 12(b) show that when the pump pulse width is 500 μs, the beam quality factors of the free-running and narrow-linewidth idler light are $M^2 = 1.91$ and 1.69, respectively. Compared with the free-running mode, the spatial quality of the mid-IR idler beam in the narrow-linewidth mode is improved.

5. Conclusion

This paper introduces a high-energy, narrow-linewidth 3.8-μm SOPO based on Nd:MgO:PPLN crystals with a repetition rate of 100 Hz. A mathematical model based on rate equations for the EOQ-SOPO system was established, simulating the temporal evolution of the

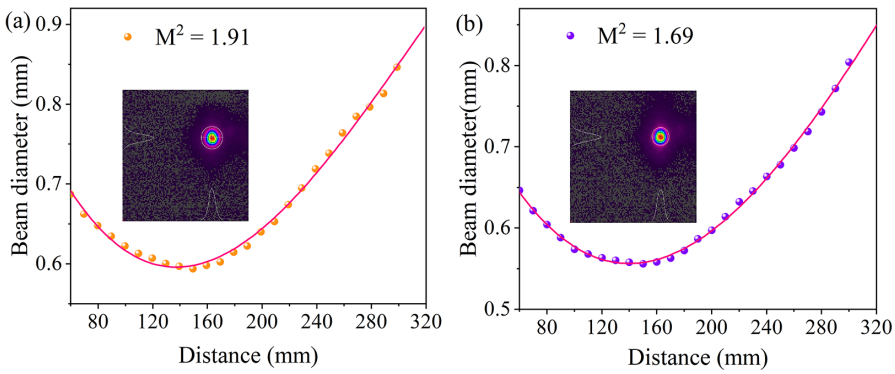

Figure 12. Beam quality of the mid-IR idler beam for a pump pulse width of 500 μs: (a) free running; (b) narrow linewidth.

https://doi.org/10.1017/hpl.2025.10052 Published online by Cambridge University Press

upper-level population and three-wave photon numbers under pulse pumping with EOQ-switching. The temporal characteristics of the three waves were experimentally verified. In the experiments, the output characteristics of 1084-nm fundamental light under various pump pulse widths were explored. By placing an F-P etalon in the fundamental cavity and adjusting its angle to 3.2°, narrow-linewidth fundamental light output was achieved. This provided the basis for experimental research on mid-IR idler light output. In the 100-Hz EOQ-SOPO system, the wavelength of free-running idler light ranged from 3845.03 to 3838.4 nm, with linewidths between 0.833 and 1.157 nm and single-pulse energies between 2.61 and 6.85 mJ under different pump pulse widths. Finally, narrow-linewidth idler light was achieved using an indirect compression method. At a pump pulse width of 500 μs, narrow-linewidth idler light at 3838.2 nm was achieved, with a single-pulse energy of 4.71 mJ, linewidth of 0.412 nm, pulse width of 4.78 ns and peak power of 985 kW. The beam quality was $M^2 = 1.69$. At a pump pulse width of 200 μs, narrow-linewidth idler light at 3845.2 nm was achieved, with a linewidth of 0.212 nm, single-pulse energy of 1.77 mJ and pulse width of 7.08 ns. This study provides valuable technical insights for developing high-quality mid-IR pulsed laser sources characterized by high energy, narrow linewidth and practicality, offering critical guidance for the optimization and application of mid-IR lasers.

Acknowledgements

This project was supported by the National Natural Science Foundation of China (Grant Nos. 62275031 and U24A2045) and the Natural Science Foundation of Jilin Province (Grant No. 20240302023GX).

References

1. B. Bruneteau, B. Faure, J. Debray, G. Souhaité, P. Segonds, H. Ishizuki, T. Taira, and B. Boulanger, Opt. Lett. **48**, 3669 (2023).
2. J. Q. Zhao, Y. W. Chen, D. Q. Ouyang, M. Q. Liu, C. B. Li, X. Wu, X. W. Xiong, L. Q. Mo, M. Wang, X. Liu, Q. T. Lv, and S. C. Ruan, Opt. Express **32**, 8364 (2024).
3. H. Wu, W. Wang, B. Hu, Y. Li, K. Tian, R. Ma, C. Li, J. Liu, J. Yao, and H. Liang, Photonics Res. **11**, 808 (2023).
4. C. Xi, P. Wang, X. Li, and Z. Liu, High Power Laser Sci. Eng. **7**, e67 (2019).
5. A. Schliesser, N. Picqué, and T. W. Hänsch, Nat. Photonics **6**, 440 (2012).
6. J. Liang, J. Xu, Y. Ke, S. Li, J. He, Y. Guo, Y. Zhang, X. Ma, J. Ye, X. Li, J. Leng, and P. Zhou, Photonics Res. **12**, 1593 (2024).
7. L. Schmid, F. Kadriu, S. Kuppel, M. Floess, T. Steinle, and H. Giessen, AIP Adv. **14**, 105328 (2024).
8. L. Guo, Y. Yang, S. Zhao, T. Li, W. Qiao, B. Ma, H. Nie, S. Ye, R. Wang, B. Zhang, K. Yang, and J. He, Opt. Express **28**, 32916 (2020).
9. D. S. Boyd and F. Petitcolin, Int. J. Remote Sens. **25**, 3343 (2004).
10. A. Geiger, E. Degtiarev, W. Farr, and R. Richmond, Proc. SPIE **3380**, 63 (1998).
11. Y. Cai, Y. Chen, X. Xin, K. Huang, and E. Wu, Photonics Res. **10**, 2614 (2022).
12. H. Bekman, J. van den Heuvel, F. van Putten, and R. Schleijpen, Proc. SPIE **5615**, 27 (2004).
13. H. D. Tholl, Proc. SPIE **10797**, 1079702 (2018).
14. Y. F. Peng, X. B. Wei, G. Xie, J. R. Gao, D. M. Li, and W. M. Wang, Laser Phys. **23**, 055405 (2013).
15. K. Wang, M. Y. Gao, S. H. Yu, J. Ning, Z. D. Xie, X. J. Lv, G. Zhao, and S. N. Zhu, Sci. Rep. **11**, 5079 (2021).
16. L. Wang, W. Chen, I. B. Divliansky, V. Pasiskevicius, O. Mhibik, K. M. Moelster, A. Zukauskas, and V. Petrov, J. Opt. Soc. Am. B **41**, E15 (2024).
17. Y. Peng, W. Wang, X. Wei, and D. Li, Opt. Lett. **34**, 2897 (2009).
18. J. Saikawa, M. Fujii, H. Ishizuki, and T. Taira, Opt. Lett. **31**, 3149 (2006).
19. M. Schellhorn, G. Spindler, and M. Eichhorn, Opt. Express **26**, 1402 (2018).
20. H. Ishizuki and T. Taira, in *Advanced Solid State Lasers*, OSA Technical Digest (online) (Optica Publishing Group, 2014), paper ATu4A.3.
21. J. Liu, Q. Liu, L. Huang, and M. Gong, Laser Phys. Lett. **7**, 853 (2010).
22. Q. B. Sun, H. J. Liu, N. Huang, C. Ruan, S. L. Zhu, and W. Zhao, Laser Phys. Lett. **8**, 16 (2011).
23. V. S. Serebryakov, É. Boiko, A. G. Kalintsev, A. F. Kornev, A. S. Narivonchik, and A. L. Pavlova, J. Opt. Technol. **82**, 781 (2015).
24. Q. Liu, Z. Zhang, J. Liu, and M. Gong, Infrared Phys. Technol. **61**, 287 (2013).
25. Y. Q. Fan, J. Liu, C. P. Qian, W. F. Lin, M. Y. Fan, T. Yu, X. C. Shi, and X. S. Ye, Infrared Phys. Technol. **139**, 105307 (2024).
26. Z. Zhang, Y. Zhao, H. Liu, Z. Wang, Y. Yang, Y. Yu, and G. Jin, Infrared Phys. Technol. **124**, 104234 (2022).
27. T. L. Xing, L. Wang, S. W. Hu, T. Q. Cheng, X. Y. Wu, and H. H. Jiang, Opt. Express **25**, 31810 (2017).
28. G.-R. Lv, L. Guo, H.-P. Xu, X.-A. Dou, H. Kong, Y.-L. Yang, J.-Q. Wen, J.-T. Bian, Q. Ye, X.-Q. Sun, and K.-J. Yang, Opt. Laser Technol. **160**, 109064 (2023).
29. Y. H. Chen, W. K. Chang, N. Hsu, C. Y. Chen, and J. W. Chang, Opt. Lett. **37**, 2814 (2012).
30. X. Wei, X. Ye, X. Xu, H. Ren, J. Liu, D. Sun, H. Liu, L. Zhang, and W. Wang, Opt. Laser Technol. **151**, 108062 (2022).
31. W. Wang, X. Jin, M. Sun, R. Zhao, Z. Wang, H. Liu, and Y. Yu, Infrared Phys. Technol. **140**, 105415 (2024).
32. R. Zhao, S. Wu, H. Liu, Z. Wang, C. Wang, Y. Yu, and G. Jin, Opt. Express **32**, 29316 (2024).
33. J. Falk, J. Yarborough, and E. Ammann, IEEE J. Quantum Electron. **7**, 359 (1971).
34. T. Debuisschert, J. Raffy, J. P. Pocholle, and M. Papuchon, J. Opt. Soc. Am. B **13**, 1569 (1996).
35. Z. Liu, Q. Wang, X. Zhang, Z. Liu, J. Chang, H. Wang, S. Fan, W. Sun, G. Jin, X. Tao, S. Zhang, and H. Zhang, Appl. Phys. B **92**, 37 (2008).
36. F. Bai, Q. P. Wang, Z. J. Liu, X. Y. Zhang, X. B. Wan, W. X. Lan, G. F. Jin, X. T. Tao, and Y. X. Sun, Opt. Express **20**, 807 (2012).
37. D. Z. Wang, D. H. Sun, X. L. Kang, Y. H. Sang, B. X. Yan, H. Liu, and Y. Bi, Opt. Express **23**, 17727 (2015).
38. O. Gayer, Z. Sacks, E. Galun, and A. Arie, Appl. Phys. B **91**, 343 (2008).

https://doi.org/10.1017/hpl.2025.10052 Published online by Cambridge University Press